

UWB Beam-Based Local Diffraction Tomography—Part I: Phase-Space Processing and Physical Interpretation

Ram Tuvi, Ehud Heyman^{ID}, *Life Fellow, IEEE*, and Timor Melamed^{ID}, *Senior Member, IEEE*

Abstract—In this two-part article, we study the ultrawideband beam-based schemes for tomographic inverse scattering. The theory utilizes discrete phase-space sets of beam waves, which constitute overcomplete frames everywhere in the propagation domain, and thus can be considered as a local alternative to the conventional plane-wave or Green’s function integrals used in conventional diffraction tomography. Specifically, we formulate two inversion schemes, a multi-frequency domain scheme, and a time domain scheme. The former utilizes isodiffracting Gaussian beams, while the latter utilizes isodiffracting pulsed beams. Both schemes consist of two phases: In the preprocessing phase, the scattering data are expanded as a sum of beams whose amplitudes, referred to as the “beam-domain data,” are extracted from the data using local beam-based transforms. In the imaging phase, the beam data are backpropagated and used for local reconstruction. In this Part I we discuss the preprocessing phase. We define the beam-based transforms, and then use the Born approximation to establish a cogent physical interpretation of the beam-domain data. Specifically, we show that these data are related to the local Radon transform of the medium, which is interpreted physically as a local Snell’s law. This relation will be used in Part II to reconstruct the medium.

Index Terms—Beam summation methods, diffraction tomography (DT), inverse scattering.

NOMENCLATURE

List of Acronyms

UWB	Ultrawideband.
GB	Gaussian beam.
PB	Pulsed beam.
ID	Isodiffracting.
FD	Frequency domain.
TD	Time domain.
WFT	Windowed Fourier transform.
WRT	Windowed Radon transform.

Manuscript received December 15, 2018; revised November 27, 2019; accepted April 25, 2020. Date of publication May 12, 2020; date of current version October 6, 2020. This work was supported by the Israeli Science Foundation (ISF) under Grant 412/15 and Grant 1111/19. (*Corresponding author: Ehud Heyman.*)

Ram Tuvi was with the School of Electrical Engineering, Tel Aviv University, Tel Aviv 69978, Israel. He is now with the Jackson School of Geosciences, Institute for Geophysics, The University of Texas at Austin, Austin, TX 78758 USA (e-mail: ram.tuvi@gmail.com).

Ehud Heyman is with the School of Electrical Engineering, Tel Aviv University, Tel Aviv 69978, Israel (e-mail: heyman@tau.ac.il).

Timor Melamed is with the School of Electrical and Computer Engineering, Ben-Gurion University of the Negev, Be’er Sheva 8410501, Israel (e-mail: timormel@bgu.ac.il).

Color versions of one or more of the figures in this article are available online at <http://ieeexplore.ieee.org>.

Digital Object Identifier 10.1109/TAP.2020.2992806

BF	Beam frame.
PBF	Pulsed-beam frame.
DT	Diffraction tomography.

I. INTRODUCTION

THIS two-part article is concerned with UWB beam-based formulations for tomographic inverse scattering [Fig. 1(a)]. The theory utilizes discrete phase-space sets of beam waves, which constitute overcomplete frames¹ everywhere in the propagation domain, and thus provide a local alternative to the conventional plane-wave or Green’s function expansion sets used in conventional DT. Specifically, we formulate two UWB inversion schemes, a multifrequency scheme and a TD scheme, which are used, respectively, when the data are expressed in the multi-FD or directly in the TD. The former utilizes ID-GB waves, while the latter utilizes ID-PB waves. The methods are structured upon the “BFs” and the “PBFs” presented in [1], hence for the sake of conciseness and completeness, we make extensive reference throughout these articles to specific equations and figures in [1], denoting them by the prefix §.

As schematized in Fig. 1(b), beam-based inversion schemes consist of two phases. In the preprocessing phase, the scattered field is expanded as a sum of beam propagators² whose amplitudes, referred to as the “beam-domain data,” are extracted from the measured field using local beam-based transforms. Then, in the imaging phase, these beams are backpropagated to reconstruct the scattering medium. Actually, as illustrated, one needs to process and backpropagate only those beams that pass through or near a given sub-domain of interest (DoI). This Part I is concerned with the preprocessing phase, where, using the weak scattering (Born) approximation for the scattered field, we establish a local relation between the scattering medium and the beam-domain data. The results are then used in Part II [2] that addresses the imaging phase.

The linearized “data-object relation” which constitutes the basis of DT is usually expressed as a relation between the K -space distribution of the scattering medium and the angular spectrum of the scattered field (see a brief review in Section III-A). Thus, this K -space distribution can be reconstructed by measuring the scattered field due to multiple

¹A “frame” over an inner-product space is a generalization of a basis to sets that may be linearly dependent. Frames provide a redundant, stable way of representing functions in that space.

²We use the generic term “beams” for both the ID-GB or the ID-PBs which are our favorable propagators in the FD and TD formulations, respectively.

illumination directions and/or frequencies, and the medium is then recovered via an inverse transform to the configuration domain. This spectral reconstruction approach can be circumnavigated via the “filtered backpropagation” algorithm [3]–[5] where the measured field for each illumination is spatially filtered and then backpropagated to the target domain. Aggregating the backpropagated fields due to all the illuminations yields the reconstructed medium. Further details can be found in [6] and [7].

For short pulse data, it might be preferable to use the TD-DT derived in [8]. The theory, which is briefly reviewed in Section III-B, establishes a direct relationship between the angular spectrum of the time-dependent scattered field and the Radon transform of the medium. Physically, this relation can be regarded as a *generalized Snell’s law*. The medium is then reconstructed via an inverse Radon transform of the backpropagated transient data.

A. Overall Goal of this Two-Part Article

The overall goal of this article is to formulate localized DT imaging schemes, in both the multi-FD and the TDs, using collimated beam-waves for data processing and backpropagation. The advantages of the beam approach are as follows:

- 1) focusing the data for local imaging within any given DoI;
- 2) reduced complexity, since it accounts only for the beam basis-functions that cover the DoI;
- 3) reduced noise level, since data and noise arriving from other regions are a priori filtered out;
- 4) possible extensions for backpropagation and imaging over inhomogeneous backgrounds.

Because of these properties, beam processing methods have been explored recently for inverse scattering in various disciplines including electromagnetics [9]–[15], geophysics, and underwater acoustics [16]–[27].

Without getting into a thorough comparison with these schemes, we outline the key features of the beam-based inverse scattering method presented in this article.

- 1) It is structured upon the UWB phase-space beam-summation (UWB-PS-BS) method [30], [31]. In this approach, the field is rigorously expanded over an *overcomplete phase-space* set of Gaussian beams, identified by their initiation points, directions, and times, referred to as the *beam lattice*, as schematized in Fig. 1.
- 2) The theory is UWB in the following sense.
 - a) The beam lattice is *frequency independent*, implying that the beam trajectories need to be calculated once and then used for all frequencies. In the conventional Gabor-series expansions, on the other hand, the beam lattice changes with the frequency.
 - b) It utilizes the ID-GB whose propagation parameters can be calculated analytically in inhomogeneous media. Furthermore, these parameters have an “isodiffracting” frequency scaling, implying that they are *frequency independent* and hence need to be calculated only once and then used for all frequencies [28], [29].
 - c) Properties (2a) and (2b) imply that the theory may be formulated directly in the TD using ID-PB

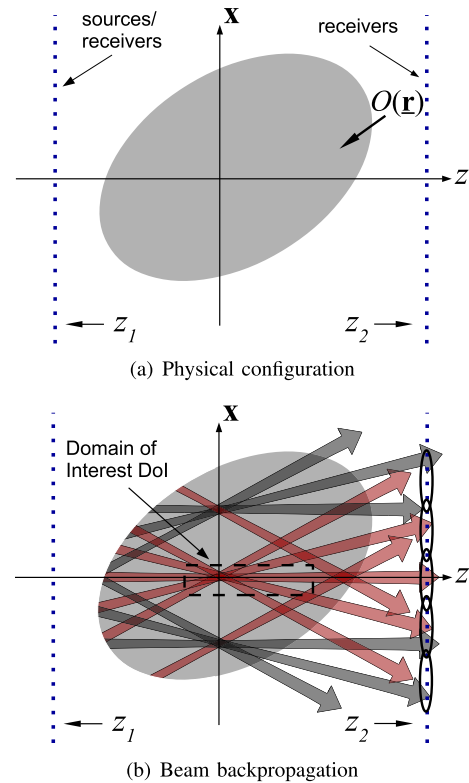


Fig. 1. Conceptual sketch of the beam-based inverse scattering scheme. (a) Unknown medium $O(\mathbf{r})$ is located between the measurement planes $z = z_{1,2}$. (b) Measured data (we sketch only the data at z_2) are transformed to the beam domain, and then backpropagated to the target domain, but only those beams passing through the DoI, depicted in red, are considered in the reconstruction process. (a) Physical configuration. (b) Beam backpropagation.

propagators. An important property of the ID-PB is that they maintain their analytic structure through propagation in inhomogeneous media, and hence may be regarded as eigenwavepacket solutions of the wave equation [28].

- 3) The expansion coefficients, referred to as the *beam-domain data*, are calculated in the preprocessing phase via windowed phase-space processing of the scattering data [see (17) and (24)] that extract the local spectral properties of the field, e.g., the local directions and times of arrival.
- 4) The beam-domain data are shown to be directly related to local features of the interrogated medium (Section V-C). This data–medium relationship has a cogent physical interpretation in terms of a local Radon transform (LRT) of the medium and a local generalized Snell’s reflection law.
- 5) The reasons for using an overcomplete expansion are as follows.
 - a) The expansion coefficients are local and stable, whereas in the conventional Gabor-based representations, they are notoriously nonlocal and unstable [33].
 - b) It adds the degree of freedom that is needed to construct the frequency-independent beam lattice in item 2a [30].

- c) It offers the wave-modeler degrees of freedom in choosing the most appropriate beam-set for a given problem.
- 6) Finally, the formulation is structured upon the BF theory, introduced originally in the context of propagation through randomly fluctuating media [34], [35]. As has been proved there, the phase-space beam sets mentioned earlier constitute frames not only over the aperture plane but everywhere in the propagation domain. In the present context of inverse scattering, these BFs are used not only to expand the data as in item 5 but also for local expansion of the medium inhomogeneities and then for local reconstruction. The reader is referred to [1] where the BF theory is presented in a unified FD and TD formulation.

It is worth noting that our method has recently been successfully applied for seismic imaging in [36].

In this article, we apply the BF concept to formulate the beam-based local tomographic inverse scattering algorithms illustrated in Fig. 1. This article is concerned with the pre-processing phase. We define the beam-based transforms that extract the “beam-domain data” from the measured data, both in the FD or in the TD. Then, using the Born approximation, we derive a cogent physical model of the TD data and show that it is related to the “LRT” of the medium. This relation will be used in Part II [2] to reconstruct the medium by backpropagating these beams.

The presentation starts in Section II with a brief description of the problem and then proceeds in Section III with a review of the conventional DT formulations in the frequency and in the TDs. The beam-based processing of the scattering data are then presented in Sections IV and V for the FD and TD formulations, respectively. In each section, we first define the formal processing tools and then explore the local content of the beam data within the Born approximation. To simplify the presentation, we utilize formal expressions for the frame elements (the beam propagators); the readers are referred to Appendixes §A–§C for explicit expressions for the ID-GB and ID-PB frame elements in 3-D and 2-D configurations. These expressions are used in the numerical examples here and in Part II, where we also outline the considerations for choosing the beam-expansion parameters.

II. PROBLEM DESCRIPTION

Referring to Fig. 1(a), we consider a lossless, nondispersive medium with wavespeed $v(\mathbf{r})$ in a 3-D coordinate frame, which is embedded in a uniform medium v_0 . The medium is characterized by the “object function”

$$O(\mathbf{r}) = n^2(\mathbf{r}) - 1, \quad n(\mathbf{r}) = \frac{v_0}{v(\mathbf{r})} = \text{refractive index.} \quad (1)$$

The medium is located between two planes, $z = z_1 < 0$ and $z_2 > 0$ whereon the source and receiver arrays are located. In our implementation, the medium is probed by an array of sources located on the $z = z_1$ plane, and the scattering data are measured by receiver arrays on the z_1 and/or z_2 planes, henceforth tagged by the index $j = 1, 2$, respectively. These data are organized in a matrix \mathbf{D} whose qp element is the field

measured at receiver q due to a unit excitation at source p . Henceforth, we designate the 3-D coordinates as $\mathbf{r} = (\mathbf{x}, z)$, where $\mathbf{x} = (x_1, x_2)$ are the coordinates transverse to the z -axis.

The data are measured over a wide frequency band $\Omega = [\omega_{\min}, \omega_{\max}]$. It may be measured either in the multi-FD, in a frequency by frequency approach, or in the short-pulse domain. Henceforth, frequency and TD constituents are related via the Fourier transform

$$\hat{u}(\mathbf{r}, \omega) = \int_{-\infty}^{\infty} dt e^{i\omega t} u(\mathbf{r}, t) \quad (2)$$

where $\hat{\cdot}$ is used to denote FD constituents.

III. REVIEW OF PLANE-WAVE-BASED DT

We briefly review the FD and TD tomographic inverse scattering formulations (Sections III-A and III-B, respectively). Referring to the configuration in Fig. 2(a), we consider both the “angular diversity” and the “frequency diversity” formulations, where the data are measured for several illumination directions $\hat{\mathbf{k}}^i$, or over a wide frequency band for a given $\hat{\mathbf{k}}^i$.

A. FD Formulation of DT

1) *Problem Setup:* Referring to Fig. 2(a), the unknown object $O(\mathbf{r})$ is illuminated by a time-harmonic plane wave

$$\hat{u}^i(\mathbf{r}, \omega) = e^{ik\hat{\mathbf{k}}^i \cdot \mathbf{r}}, \quad k = \omega/v_0, \quad (3)$$

with $\hat{\mathbf{k}}^i = (\boldsymbol{\xi}^i, \zeta^i) = (\sin \theta^i \cos \phi^i, \sin \theta^i \sin \phi^i, \cos \theta^i)$ being the unit-vector that defines the plane wave direction, and (θ^i, ϕ^i) are the spherical angles with respect to the z -axis [see $(\boldsymbol{\xi}, \zeta)$ in (4)]. Here and henceforth, unit vectors are denoted by an over-circle.

The scattering data measured on the $z_{1,2}$ planes are denoted as $\hat{u}_j^s(\mathbf{x}, \omega)$ with $j = 1, 2, \dots$. The plane-wave spectrum of these data is defined by

$$\hat{u}_j^s(\boldsymbol{\xi}, \omega) = e^{\pm ik\zeta z_j} \int d^2x \hat{u}_j^s(\mathbf{x}, \omega) e^{-ik\boldsymbol{\xi} \cdot \mathbf{x}} \quad (4)$$

where, here and henceforth, upper and lower signs correspond to $j = 1$ and 2 , respectively. Here, $\boldsymbol{\xi} = (\xi_1, \xi_2) = \sin \theta (\cos \phi, \sin \phi)$ are the spectral wave-numbers associated with (x_1, x_2) and $\zeta = \sqrt{1 - \boldsymbol{\xi} \cdot \boldsymbol{\xi}}$, where $\text{Im} \zeta \geq 0$, is the spectral wavenumber in the z -direction. Since we are interested in UWB formulations, we use the frequency-normalized spectral coordinates $\boldsymbol{\xi} = \mathbf{k}_x/k$ that define the plane-wave directions (θ, ϕ) in a frequency independent manner. Here and henceforth (also in the TD), spectral functions are denoted by tilde $\tilde{\cdot}$. In (4), we also introduce the extra term $e^{\pm ik\zeta z_j}$ that normalizes the spectral plane waves with respect to the $z = 0$ plane instead of the $z = z_{1,2}$ planes (i.e., their phase centers are at the origin).

The scattered fields for $z < z_1$ and for $z > z_2$ can be expressed now in terms of data \hat{u}_j^s , namely

$$\hat{u}_j^s(\mathbf{r}, \omega) = \left(\frac{k}{2\pi}\right)^2 \int d^2\xi \hat{u}_j^s(\boldsymbol{\xi}, \omega) e^{ik\hat{\mathbf{k}}_j \cdot \mathbf{r}} \quad (5)$$

where $\hat{\mathbf{k}}_j = (\boldsymbol{\xi}, \mp \zeta) = (\sin \theta_j \cos \phi_j, \sin \theta_j \sin \phi_j, \cos \theta_j)$ are the outgoing plane wave directions for $j = 1, 2$, and

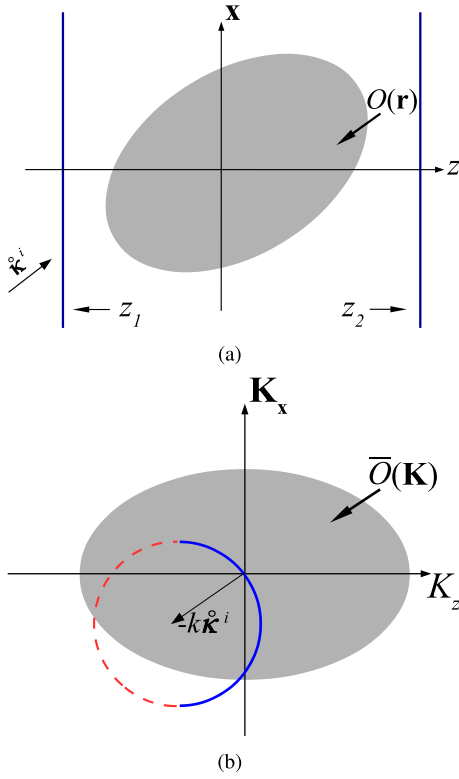


Fig. 2. DT in the spatial and spectral domains. (a) Object illuminated by the plane wave (3) propagating in the $\hat{\mathbf{k}}^i$ direction. (b) K -space representation of (7). The scattered field $\hat{u}_j^s(\boldsymbol{\xi})$ is mapped to $\bar{O}(\mathbf{K})$ on the shifted Ewald sphere $\mathbf{K} = k(\hat{\mathbf{k}}_j - \hat{\mathbf{k}}^i)$. The dashed- and solid-line hemispheres correspond to data measured on the $j = 1, 2$ planes, respectively.

(θ_j, ϕ_j) are the conventional spherical angles with respect to the $+z$ -axis. The spectral ranges $|\boldsymbol{\xi}| < 1$ and $|\boldsymbol{\xi}| > 1$ are defined as the propagating and the evanescent spectra, respectively. The following tomographic formulation utilizes only the propagation spectrum data in the range $|\boldsymbol{\xi}| < 1$. Adding the evanescent spectrum data to improve the reconstruction suffers from low signal-to-noise ratio [39] and is not utilized in this article.

2) *Basic DT Identity*: In the weak scattering regime, the scattered field may be expressed by the first order Born approximation

$$\hat{u}^s(\mathbf{r}) \simeq k^2 \int_V d^3r' \hat{u}^i(\mathbf{r}') O(\mathbf{r}') \hat{G}(\mathbf{r}, \mathbf{r}') \quad (6)$$

where $\hat{G}(\mathbf{r}, \mathbf{r}') = (e^{ik|\mathbf{r}-\mathbf{r}'|})/(4\pi|\mathbf{r}-\mathbf{r}'|)$ is the free space Green's function.

Applying (4) to (6), we find (see derivation in Appendix A) that the spectral representation of the data is related to the object function via

$$\hat{u}_j^s(\boldsymbol{\xi}) \simeq \frac{k}{-2i\zeta} \bar{O}(\mathbf{K}) \Big|_{\mathbf{K}=k(\hat{\mathbf{k}}_j - \hat{\mathbf{k}}^i)}, \quad |\boldsymbol{\xi}| < 1, \quad (7)$$

where the unit vectors $\hat{\mathbf{k}}_j$ and $\hat{\mathbf{k}}^i$ are defined in (5) and (3), respectively, and

$$\bar{O}(\mathbf{K}) = \int d^3r O(\mathbf{r}) e^{-i\mathbf{K}\cdot\mathbf{r}}, \quad \mathbf{K} = (K_1, K_2, K_z), \quad (8)$$

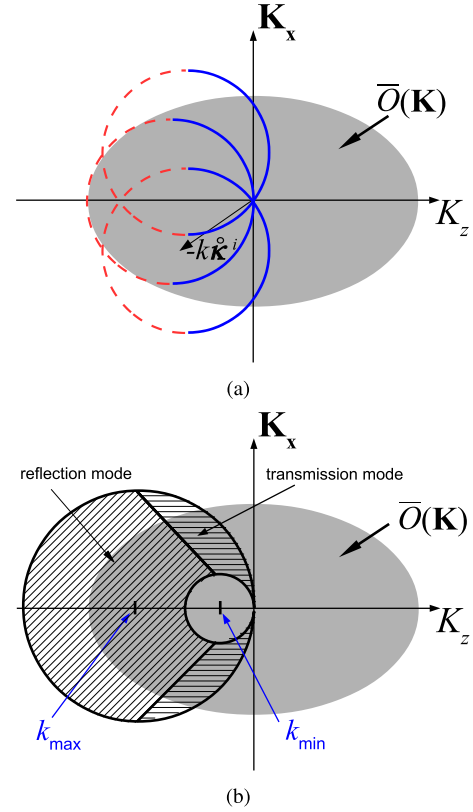


Fig. 3. K -space reconstruction. (a) Angular diversity reconstruction: changing the direction of illumination $\hat{\mathbf{k}}^i$ provides coverage of the K -space within a sphere of radius $2k$. (b) Frequency diversity reconstruction: changing the excitation frequency for a single illumination direction $\hat{\mathbf{k}}^i$ (here, $\hat{\mathbf{k}}^i = \hat{\mathbf{z}}$) provides the K -space coverage indicated, where the areas denoted by the slanted and vertical hatching correspond to data measured on the $j = 1$ and $j = 2$ plane, respectively.

is the K -domain representation of O . Equation (7) is the *basic DT identity*. It implies that the amplitude of the scattered plane waves in the $\hat{\mathbf{k}}_j$ direction is determined by the value of $\bar{O}(\mathbf{K})$ at $\mathbf{K} = k(\hat{\mathbf{k}}_j - \hat{\mathbf{k}}^i)$. Referring to Fig. 2(b), these points are located on a sphere of radius k that is centered at $\mathbf{K} = -k\hat{\mathbf{k}}^i$, referred to as the *shifted Ewald sphere*. As follows from the definition of the spectral directions $\hat{\mathbf{k}}_j$ in (5), the dashed and the solid-line hemispheres correspond to data measured on the $j = 1, 2$ planes, respectively (i.e., reflection and transmission data). Relation (7) implies that $\bar{O}(\mathbf{K})$ can be recovered by measuring the scattered fields \hat{u}_j^s for various values of $\hat{\mathbf{k}}^i$ or ω (see Sections III-A3 and III-A4, respectively). The latter approach can actually be implanted directly in the TD (see Section III-B).

3) *Object Reconstruction via Angular Diversity (Monochromatic Tomography)*: Referring to Fig. 3(a), $\bar{O}(\mathbf{K})$ may be reconstructed by measuring the scattered field for several illumination directions $\hat{\mathbf{k}}^i$, such that each direction determines the value of $\bar{O}(\mathbf{K})$ on the corresponding shifted Ewald sphere via (7). $O(\mathbf{r})$ is then obtained via an inverse Fourier transform of (8). Further details and references concerning this spectral reconstruction approach can be found in [6, Ch. 8] and [7, Ch. 9].

An alternative reconstruction approach is provided by the “filtered backpropagation” algorithm [3]–[5]. Here, the

scattered field measured is spatially filtered and then back-propagated to the target domain such that the reconstructed $O(\mathbf{r})$ is obtained by aggregating the backpropagated fields due to all the illuminations. Further details and references can be found in [6] and [7].

4) *Object Reconstruction via Frequency Diversity (UWB Tomography)*: An alternative way to cover the K -space is to change the excitation frequency, thereby changing the radius of the shifted Ewald sphere in (7). This can be done either by performing multimono-chromatic experiments, or by using the UWB, short-pulse excitation. The data can then be analyzed in the multi-FD or directly in the TDs as in Section III-B.

The FD approach is illustrated in Fig. 3(b). For simplicity, the interrogating plane wave propagates in the $+z$ -direction and the frequency is swept in the range $\Omega = [\omega_{\min}, \omega_{\max}]$. Fig. 3(b) depicts the K -space coverage by the shifted Ewald spheres as their radii vary between k_{\min} and k_{\max} . One finds that the reflection data at z_1 cover a $\pi/4$ cone about the $-K_z$ -axis, truncated between $K = k_{\min}$ and $K = k_{\max}$ [diagonal hatching in Fig. 3(b)], whereas the transmission data at z_2 cover the remaining K -space zone (horizontal shading). If O is real, then $\tilde{O}(-\mathbf{K}) = \tilde{O}^*(\mathbf{K})$ so that it is sufficient to cover only the half-space $K_z < 0$ as in Fig. 3(b). Otherwise, the interrogation should be in both $\pm z$ -directions.

Denoted by $\tilde{O}_j(\mathbf{K})$ the parts of $\tilde{O}(\mathbf{K})$ in Fig. 3(b) that are recovered by the data $\hat{u}_j^s(\mathbf{x})$ on the z_j plane, and by $\check{O}_j(\mathbf{r})$ the corresponding reconstructed ‘‘partial’’ images, it follows that \check{O}_1 and \check{O}_2 correspond, essentially, to the longitudinal and transversal variations of O (see also the Radon transform interpretation in Fig. 4). In many cases, one has access to scattering data on one plane only, leading to partial reconstruction, but if one data from both planes, then the ‘‘full reconstruction’’ is given by $\check{O}(\mathbf{r}) = \check{O}_1(\mathbf{r}) + \check{O}_2(\mathbf{r})$.

From Fig. 3(b), the single aspect-angle UWB approach is mainly effective for quasi-stratified media in reflection tomography; in this case, $\check{O}(\mathbf{r}) \approx \check{O}_1(\mathbf{r})$.

A major difficulty, however, is the lack of data regarding \tilde{O} for $|\mathbf{K}| < k_{\min}$ which is related to the average of $O(\mathbf{r})$. However, choosing

$$k_{\min} < 1/L \quad (9)$$

where L is the overall size of the object along the z -axis, and then one may infer the value of \tilde{O} near $|\mathbf{K}| = 0$ from the data at k_{\min} . Likewise, we note from Fig. 3(b) that the largest values of K_z that can be recovered is $2k_{\max}$, so that the axial resolution is limited by

$$\delta_z \simeq \pi/k_{\max}. \quad (10)$$

This determines the choice of the highest frequency k_{\max} .

B. TD-DT: Generalized Snell’s Law

In Section III-A4, the UWB tomography has been performed in the multi-FD, in a discrete frequency-by-frequency approach. For short pulse data, it might be preferable to perform the reconstruction directly in the TD using the theory developed in [8] which is briefly reviewed here. We consider TD scattering due to an incident pulsed plane wave

$$u^i(\mathbf{r}, t) = F(t - v_0^{-1} \hat{\boldsymbol{\kappa}}^i \cdot \mathbf{r}) \quad (11)$$

which is the TD counterpart of the time-harmonic plane wave (3), where $F(t)$ is a short pulse that provides the proper spectral resolution discussed in (9) and (10). In the following, we also present simplified expressions for $F(t) \simeq \delta(t)$.

The TD-DT relation is expressed in the spectral domain. The plane-wave spectrum $\tilde{u}_j^s(\boldsymbol{\xi}, \tau)$ of the scattering data $u_j^s(\mathbf{x}, t)$, obtained by transforming (4) to the TD, is given by [37]

$$\tilde{u}_j^s(\boldsymbol{\xi}, \tau) = \int d^2x u_j^s[\mathbf{x}, \tau + v_0^{-1}(\boldsymbol{\xi} \cdot \mathbf{x} \mp \zeta z_j)]. \quad (12)$$

As discussed in (§23) and Fig. §7, this expression extracts from u_j^s the time-dependent plane waves $\tilde{u}_j^s(\boldsymbol{\xi}, \tau)$ that propagate in the spectral directions $\hat{\boldsymbol{\kappa}}_j$ of (5), with τ being the time-variable of these plane waves. As discussed in (4), the term $\mp \zeta z_j$ normalizes the spectral plane waves so that they are referenced to the origin.

The TD-DT identity has been derived directly in the TD [8]. Here, however, we sketch the FD route, starting with the FD identity (7). We multiply this expression by the excitation spectrum $\hat{F}(\omega)$ and invert into the TD via (2). The left-hand side yields $\tilde{u}_j^s(\boldsymbol{\xi}, \tau)$ of (12). For the right-hand side, we use the inverse of (8), thus obtaining

$$\tilde{u}_j^s(\boldsymbol{\xi}, \tau) = \int d^3r \frac{1}{-2v_0\zeta} O(\mathbf{r}) \hat{F}[\tau + v_0^{-1}(\hat{\boldsymbol{\kappa}}_j - \hat{\boldsymbol{\kappa}}^i) \cdot \mathbf{r}] \quad (13)$$

where $\hat{F}(t) \stackrel{\text{def}}{=} dF(t)/dt$. In order to gain physical insight, we define $\hat{\mathbf{s}}_j$ as the unit vector that bisects the angle γ between $-\hat{\boldsymbol{\kappa}}^i$ and $\hat{\boldsymbol{\kappa}}_j$ [see Fig. 4(a) and (b)], and define

$$\hat{\mathbf{s}}_j = \frac{\hat{\boldsymbol{\kappa}}_j - \hat{\boldsymbol{\kappa}}^i}{2 \cos(\gamma/2)}, \quad p_j = -\frac{v_0\tau}{2 \cos(\gamma/2)}. \quad (14)$$

Assuming also $F(t) \simeq \delta(t)$, (13) reduces to

$$\tilde{u}_j^s(\boldsymbol{\xi}, \tau) = \frac{v_0 \hat{\partial}_p}{8\zeta \cos^2 \frac{\gamma}{2}} \int d^3r O(\mathbf{r}) \delta(p_j - \hat{\mathbf{s}}_j \cdot \mathbf{r}) \quad (15a)$$

$$\stackrel{\text{def}}{=} \frac{v_0 \hat{\partial}_p}{8\zeta \cos^2 \frac{\gamma}{2}} \mathcal{R}\{O\}[\hat{\mathbf{s}}_j, p_j] \quad (15b)$$

where $\mathcal{R}\{O\}$ is the Radon transform of O , representing projections of $O(\mathbf{r})$ along plans normal to the $\hat{\mathbf{s}}_j$ axis, with p_j being the coordinate along this axis. For a general F , the δ in (15a) should be replaced by F , as in (13).

Equation (15) is the TD-DT identity [8]. Referring to Fig. 4, it states that the scattered signal in the $\hat{\boldsymbol{\kappa}}_j$ direction on the left-hand side (i.e., the time-dependent plane-wave spectrum of the scattered field) is determined by the Radon transform of O along the $\hat{\mathbf{s}}_j$ axis that bisects the angle between the directions of incidence and scattering, with the spectral time τ defining the coordinate p_j along this axis via (14).

Comparing Fig. 4(a) and 4(b), we observe that the reflection data $u_1^s(\mathbf{x}, t)$ and the transmission data $\hat{u}_2^s(\mathbf{x})$ resolve, respectively, the longitudinal and transversal variations of O (recall also the discussion in Section III-A4). Note also the singularity of p_2 of (14) in the forward scattering direction $\hat{\boldsymbol{\kappa}} = \hat{\boldsymbol{\kappa}}^i$, which implies that the scattered signal cannot resolve the p coordinate in that direction.

Relation (15) has a cogent physical interpretation in terms of a *generalized Snell’s law*. This follows from the fact that the

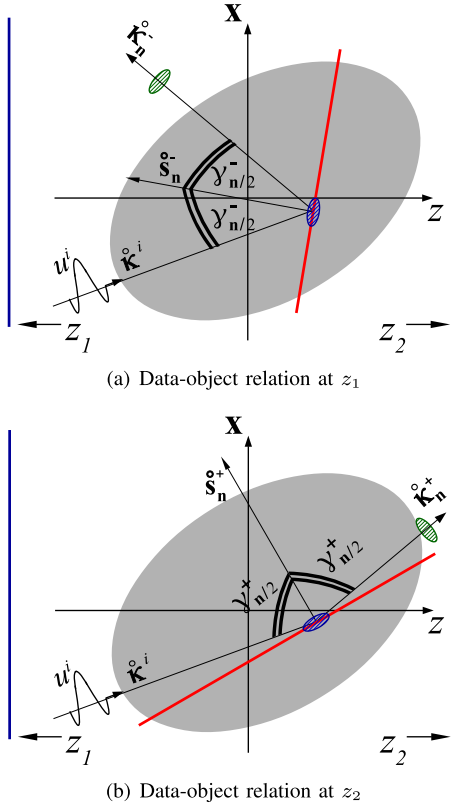


Fig. 4. TD-DT. The object-data relations illustrated in the 3-D object domain $O(\mathbf{r})$. The pulsed plane-wave formulation of Section III-B is illustrated by the planar projections, while the PB formulation of Section V-C is illustrated by the blue ellipsoidal projection and the green PB propagators. (a) Reflection data at z_1 . (b) Transmission data at z_2 .

Radon transform expresses O as an angular superposition of stratified media whose inhomogeneity along any stratification axis $\hat{\mathbf{s}}$ is $\mathcal{R}\{O\}[\hat{\mathbf{s}}, p]$, with p being the coordinate along this axis. Thus, for each $\hat{\mathbf{s}}$, the response to the incident pulsed plane wave is a reflected transient plane wave whose angle of reflection equals the angle of incidence and whose waveform is proportional to the derivative of the inhomogeneity along this axis.

The TD-DT identity implies that the Radon spectrum of O can be reconstructed via (13) so that O may be recovered via the inverse Radon transform [38]. This operation can be phrased as a *TD filtered backpropagation* [8] (see also an alternative derivation in [2, Sec. II.D]).

IV. BEAM-DOMAIN SCATTERING DATA: FD FORMULATION

As discussed in Section I, our goal is the formulation of the DT using local wave functions. In Sections IV and V, we consider the beam-domain data and its physical interpretation. In [2], these data will be used for inversion.

A. BFs

The localized DT is structured upon the theory of BFs, introduced originally in [34] and [35] in the context of rough medium scattering, and subsequently extended in [1] for radiation from UWB volume sources. For brevity and completeness,

we refer extensively to equations and figures in [1] which are identified by the prefix §.

Referring to the discussion in Section §III, the forward/backward propagating BFs are the sets of beam-waves $\{\hat{\Psi}_\mu^\pm(\mathbf{r}, \omega)\}_{\mu_p}$, with the sets $\{\hat{\Phi}_\mu^\pm(\mathbf{r}, \omega)\}_{\mu_p}$ being the associated *dual* frames. Here, the superscripts \pm indicate propagation in the $\pm z$ directions, respectively, as illustrated in Fig. §2. The beams are also tagged by the 4-index $\mu = (\mathbf{m}, \mathbf{n}) = ((m_1, m_2), (n_1, n_2)) \in \mathbb{Z}^4$ such that \mathbf{m} and \mathbf{n} define the points $\mathbf{x}_\mathbf{m} = \mathbf{m}\bar{\mathbf{x}}$ and the directions $\hat{\xi}_\mathbf{n} = \sin\theta_\mathbf{n}(\cos\phi_\mathbf{n}, \sin\phi_\mathbf{n}) = \mathbf{n}\bar{\xi}$ where the beams pass through the $z = 0$ plane (see (4) for the spherical angle definition). The index-set μ_p indicates that the set consists only of “propagating” beams such that $|\hat{\xi}_\mathbf{n}| < 1$. The parameters $(\bar{\mathbf{x}}, \bar{\xi})$ are the phase-space unit cell dimensions, satisfying the overcompleteness condition (§4). For UWB applications, these parameters are taken to be frequency independent, so that the beam-lattice is also frequency independent. The criteria for choosing these parameters are discussed in (§A2) and in the numerical examples in Section VI as well as in the examples in [1].

For UWB applications, $\hat{\Psi}_\mu^\pm(\mathbf{r}, \omega)$ are taken to be the ID-GB whose favorable properties are discussed in Section I (items 2b and 2c). The properties of these propagators in free space are summarized in Appendix §A. They are fully determined by the frequency-independent collimation length b . Once b is chosen by the wave-modeler for a given application, the lattice parameters $(\bar{\mathbf{x}}, \bar{\xi})$ are determined via (§A2), whereas we set $\nu = \nu_{\max}$ as discussed there. Once their initial conditions (direction, beamwidth, and astigmatism) are determined as outlined in Appendix §A, their frequency-independent propagation parameters in any inhomogeneous medium can be calculated analytically. Finally, we note that the properties of $\hat{\Phi}_\mu^\pm$ are similar to those of $\hat{\Psi}_\mu^\pm$, and with a proper choice of the expansion parameters, they are actually proportional as given in (§A7).

As depicted in Fig. §2(a,b), the beams in each set converge at the points $\mathbf{x}_\mathbf{m}$ in the $z = 0$ plane, where they reduce to the conventional WFT frames $\hat{\psi}_\mu(\mathbf{x})$ and $\hat{\phi}_\mu(\mathbf{x})$ in (§3) and (§7). The *BF Theorem* §1 (see in Section §III-C) states that the sets $\{\hat{\Psi}_\mu^\pm(\mathbf{r}, \omega)\}_{\mu_p}$ and $\{\hat{\Phi}_\mu^\pm(\mathbf{r}, \omega)\}_{\mu_p}$ constitute dual frames over the Hilbert space of functions with no evanescent spectrum not only at the $z = 0$ plane but actually at any plane $z = \text{const}$.

As a corollary, any function can be expanded using the forward or backward propagating frame sets. If, however, the function to be expanded is, by itself, a forward or backward propagating wavefield $\hat{u}^\pm(\mathbf{r})$, then it makes sense to expand it using the forward/backward propagating frame set, respectively. The *Coefficient Invariance Theorem* §2 in Section §III-C states that, in this case, the expansion coefficients are z independent and can be calculated at any z -plane as in (§13).

B. Beam-Domain Scattering Data

Given the scattering data $\hat{u}_j^s(\mathbf{x}; \omega)$ on the z_j planes, $j = 1$ and/or 2, the BF representation of the scattered fields $\hat{u}_j^s(\mathbf{r}, \omega)$ in the domains $z < z_1$ and $z > z_2$ is given by [see (§12)

and (§13)]

$$\hat{u}_j^s(\mathbf{r}, \omega) = \sum_{\mu \in \mu_p} \hat{A}_\mu^j(\omega) \hat{\Psi}_\mu^{\mp}(\mathbf{r}, \omega), \quad z \leq z_j \quad (16)$$

where, as noted in (4), upper and lower signs correspond to $j = 1, 2$, respectively. In view of the Coefficient Invariance Theorem (Theorem §2 in Section §III-C), the expansion coefficients, referred to as the “beam-domain data,” are extracted from the measured data \hat{u}_j^s via

$$\hat{A}_\mu^j(\omega) = \langle \hat{u}_j^s(\mathbf{x}, \omega), \hat{\Phi}_\mu^{\mp}(\mathbf{r}, \omega)|_{z_j} \rangle. \quad (17)$$

Since the processing windows $\hat{\Phi}_\mu^{\mp}|_{z_j}$ are localized about the beam-axes, with spectral tilt $\hat{\xi}_n$, the operation in (17) can be simplistically regarded as a WFT of \hat{u}_j^s over the z_j planes. Here, however, unlike the conventional WFT, the phase space windows are not simple spatial–spectral shifts of mother windows, as they contain the effect of propagation from $z = 0$ to the z_j planes, and also depend on the propagation angle $\hat{\xi}_n$ [see (§13)]. Furthermore, unlike the WFT, these windows are not structured over a Cartesian phase space lattice, but rather upon the skeleton of the beam trajectories. We, therefore, refer to (17) as the “BF transform.”

C. Beam-Domain Data Under the Born Approximation

Next, we derive an approximate model that relates \hat{A}_μ^j directly to the medium function $O(\mathbf{r})$. We note that \hat{u}_j^s is generated by the sources that are induced in the medium by the interrogating wave. These sources are given by

$$\hat{q}(\mathbf{r}, \omega) = k^2 \hat{u}(\mathbf{r}, \omega) O(\mathbf{r}) \approx k^2 \hat{u}^i(\mathbf{r}, \omega) O(\mathbf{r}) \quad (18)$$

where the second expression is the Born approximation of the sources [see (6)]. We may now use the theory of [1] for BF expansion for radiation from volume sources, according to which the expansion coefficients in (16) are given by the BF expansion (§18) of the induced sources. Thus, substituting (18) into (§18), we obtain

$$\hat{A}_\mu^j(\omega) = k^2 \int_V d^3r O(\mathbf{r}) e^{ik\hat{k}^i \cdot \mathbf{r}} [\hat{\Phi}_\mu^{\sigma\mp}(\mathbf{r})]^* \quad (19)$$

where $\hat{\Phi}_\mu^{\sigma\mp}(\mathbf{r})$ are related to $\hat{\Phi}_\mu^{\mp}(\mathbf{r})$ as in (§19). For the ID-GB frame, $\hat{\Phi}_\mu^{\sigma\mp}(\mathbf{r})$ are related to $\hat{\Psi}_\mu^{\mp}(\mathbf{r})$ via (§A8).

Relation (19) can be cast in the form

$$\hat{A}_\mu^j(\omega) = \langle O(\mathbf{r}), \hat{\Lambda}_\mu^j(\mathbf{r}, \omega) \rangle_V \quad (20)$$

$$\hat{\Lambda}_\mu^j(\mathbf{r}, \omega) = k^2 e^{-ik\hat{k}^i \cdot \mathbf{r}} \hat{\Phi}_\mu^{\sigma\mp}(\mathbf{r}, \omega) \quad (21)$$

where, as noted in (4) and (16), the upper/and lower signs correspond to $j = 1, 2$.

Equation (20) parameterizes \hat{A}_μ^j in terms of the projections of $O(\mathbf{r})$ on the “sampling windows” $\hat{\Lambda}_\mu^j(\mathbf{r})$. Thus, \hat{A}_μ^j represent integration of $O(\mathbf{r})$ along the beam axis of $\hat{\Phi}_\mu^{\mp}$. One observes that, as expected, the strongest contributions are obtained for the forward propagating beams with $\hat{\xi}_n \approx \hat{\xi}^i$ (i.e., the beam directions are near the incident wave direction); in this case, the phase $e^{-ik\hat{k}^i \cdot \mathbf{r}}$ in $\hat{\Lambda}_\mu^j$ essentially cancels the axial phase of the beams $\hat{\Phi}_\mu^{\sigma\mp}(\mathbf{r})$. Further interpretation of

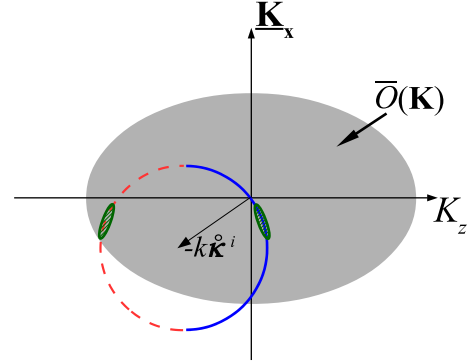


Fig. 5. K -space representation of \hat{A}_μ^j in (22). The windowing operation is performed over the shifted Ewald sphere in Fig. 2.

(20) and (21) will be given in the TD formulation (see (26) and discussion thereafter);

\hat{A}_μ^j has also an elucidating K -domain interpretation. Starting with (19) and substituting the spectral representation of $\hat{\Phi}_\mu^{\sigma\mp}(\mathbf{r})$ from (§19a), we obtain

$$\begin{aligned} \hat{A}_\mu^j &= \left(\frac{k}{2\pi}\right)^2 \int d^2\xi \frac{ik}{2\zeta} \hat{\phi}_\mu^*(\xi) \int_V d^3r O(\mathbf{r}) e^{ik\hat{k}^i \cdot \mathbf{r}} e^{-ik(\xi \cdot \mathbf{x} + \mp \zeta z)} \\ &= \left(\frac{k}{2\pi}\right)^2 \int d^2\xi \frac{ik}{2\zeta} \hat{\phi}_\mu^*(\xi) \\ &\quad \times \int_V d^3r O(\mathbf{r}) e^{-ik((\xi - \hat{\xi}^i) \cdot \mathbf{x} + (\mp \zeta - \zeta^i) z)} \end{aligned}$$

and finally, using (8) and the definition of \hat{k}_j in (5), we obtain

$$\hat{A}_\mu^j = \left(\frac{k}{2\pi}\right)^2 \int d^2\xi \frac{ik}{2\zeta} \hat{\phi}_\mu^*(\xi) \bar{O}(\mathbf{K}) \Big|_{\mathbf{K}=\hat{k}(\hat{k}_j - \hat{k}^i)} \quad (22)$$

where $\hat{\phi}_\mu(\xi) = \hat{\phi}(\xi - \hat{\xi}_n) e^{-ik\hat{\xi} \cdot \mathbf{x}_m}$ is the spectrum of the dual window $\hat{\phi}_\mu(\mathbf{x})$ [see (§6) and (§9)], with $\hat{\phi}(\xi)$ being the spectrum of the “dual window” $\hat{\phi}(\mathbf{x})$. Comparing (7) to (22), we observe that \hat{A}_μ^j are given by the values of $\bar{O}(\mathbf{K})$ over the shifted Ewald sphere, weighted by the spectral window $\hat{\phi}_\mu(\xi)$ which is localized about $\hat{\xi} \approx \hat{\xi}_n$, as illustrated in Fig. 5.

D. Section Summary

We defined the BF expansion (16) of the scattered field, where the expansion coefficients \hat{A}_μ^j , referred to as the “beam-domain data,” are extracted from the measured data \hat{u}_j^s via the windowed transform in (17). It has been shown that this operation can be regarded, rather simplistically, as a WFT of \hat{u}_j^s over the z_j planes; however, since they are not structured upon a Cartesian phase space lattice but rather upon the beam skeleton, we refer to (17) as the “BF transform.”

Then, we have demonstrated in (20) that within the Born approximation, \hat{A}_μ^j are directly related to a windowed integration of $O(\mathbf{r})$ along the respective beam axis. In (22), this relation has been expressed as a localized version of the DT identity (7) as illustrated in Fig. 5.

We defer any further interpretation of this result to the TD formulation to be considered next.

V. BEAM-DOMAIN SCATTERING DATA: TIME DOMAIN FORMULATION

The TD BF formulation has a richer and more incisive phenomenology as it resolves the data as wavepackets along beam axes. We start this section with a brief review of the PBF set of processing tools and then apply the theory to the scattering problem at hand.

A. PBFs

Referring to the discussion in Sections §V and §VI, the forward/backward propagating PBFs are the sets $\{\Psi_{\mu,s}^{\pm}(\mathbf{r}, t)\}_{\mu,p,s}$ with $\{\Phi_{\mu,s}^{\pm}(\mathbf{r}, t)\}_{\mu,p,s}$ being the associated *dual* frames. They are obtained by inverting the time-harmonic BF's $\{\hat{\Psi}_{\mu}^{\pm}(\mathbf{r}, \omega)\}_{\mu,p}$ and $\{\bar{t}\hat{\Phi}_{\mu}^{\pm}(\mathbf{r}, \omega)\}_{\mu,p}$ of Section IV-A, to the time coordinate $t - t_s$, where $t_s = s\bar{t}$ is the sampling time, $s \in \mathbb{Z}$ is an index, and \bar{t} is the sampling interval defined in (§29). These pulsed-beam waves (space-time wavepackets) propagate forward or backward, respectively, along the μ beam-axes, as illustrated by the ellipses in Fig. §2. All the parameters have the same meaning as in Section IV-A. Specifically, the 4-index $\mu = (\mathbf{m}, \mathbf{n})$ tags the points $\mathbf{x}_m = \mathbf{m}\bar{x}$ and directions $\xi_n = \mathbf{n}\bar{z}$ where the beams pass through the $z = 0$ plane at time t_s , with (\bar{x}, \bar{z}) being the phase-space unit cell dimensions discussed in Section IV-A.

Specifically, we use the ID-PB set because of its favorable properties mentioned in Section I (item 2c). They will be discussed separately in Section V-D.

As shown in Fig. §2, these PB fields converge at time $t = t_s$ at the points \mathbf{x}_m in the $z = 0$ plane, where they constitute the WRT frame-set $\{\psi_{\mu,s}(\mathbf{x}, t)\}_{\mu,p,s}$ of (§30), introduced originally in [32]. However, following the PB Frame Theorem §3 of Section §VI-C, the PB-sets $\{\Psi_{\mu,s}^{\pm}(\mathbf{r}, t)\}_{\mu,p,s}$ constitute frames not only at the $z = 0$ plane but actually at any $z = \text{const.}$ plane in the propagation domain, with $\{\Phi_{\mu,s}^{\pm}(\mathbf{r}, t)\}_{\mu,p,s}$ being their canonical dual sets, respectively. It follows that these sets may be used to expand forward or backward propagating wave fields, as was done in (§37) and (§38), or to expand volume sources as was done in (§41) and (§42). As for the FD formulation in Section IV-A, the expansion coefficients are z independent and can be calculated at any z -plane as in (§38).

B. Beam-Domain Data

As described in Section III-B, in the TD setup, we measure the scattering data $u_j^s(\mathbf{x}, t)$ on the z_j planes, $j = 1$ and/or 2 , due to the pulsed plane wave illumination (11). In view of (§37) and (§38), the PBF expansion of the scattered field for $z < z_1$ and for $z > z_2$ is given by

$$u_j^s(\mathbf{r}, t) = \sum_{\mu \in \mu_{p,s}} A_{\mu,s}^j \Psi_{\mu,s}^{\mp}(\mathbf{r}, t) \quad (23)$$

where, as noted earlier [see (4), (16), and (21)], upper and lower signs correspond to $j = 1, 2$, respectively. The expansion coefficients are extracted from the measured data u_j^s via

$$A_{\mu,s}^j = \langle u_j^s(\mathbf{x}, t), \Phi_{\mu,s}^{\mp}(\mathbf{r}, t)|_{z_j} \rangle_{(\mathbf{x}, t)} \quad (24)$$

where $\langle \cdot, \cdot \rangle_{(\mathbf{x}, t)}$ is an inner product in the (\mathbf{x}, t) domain. These coefficients are referred to as the TD beam-domain data. Note that they are the Fourier transform of $\hat{A}_{\mu}^j(\omega)$ of (17) to the time coordinate t_s up to multiplication by \bar{t} .

The processing windows in (24) are the PB fields $\Phi_{\mu,s}^{\mp}(\mathbf{r}, t)|_{z_j}$ that are centered about the μ beam-axis with spectral tilt ξ_n . The operation in (24) may therefore be regarded, quite simplistically, as a WRT of u_j^s in the (\mathbf{x}, t) domain corresponding to the z_j planes, as schematized in Fig. §7. Note though that the windows are actually more complicated than the simple schematization in Fig. §7 as they also have a propagation curvature and, unlike the WRT, they are not structured upon a Cartesian phase-space lattice, but rather upon the beam skeleton. We, therefore, refer to (24) as the PBF transform.

As discussed in Section V-D, we actually use the ID-PB windows whose properties are described there and in Appendixes §B and §C for 3-D and 2-D configurations, respectively.

C. Beam-Domain Data Under the Born Approximation: Local Generalized Snell's Law

An analytic model for $A_{\mu,s}^j$ can be derived in the single scattering approximation. We use the Born approximation of the induced sources due to the illumination (11) [see (19)]

$$\begin{aligned} q(\mathbf{r}, t) &= -v_0^{-2} \partial_t^2 u(\mathbf{r}, t) O(\mathbf{r}) \\ &\simeq -v_0^{-2} \partial_t^2 F(t - v_0^{-1} \hat{\mathbf{k}}^i \cdot \mathbf{r}) O(\mathbf{r}) \end{aligned} \quad (25)$$

where the first expression is the exact one, while in the second, we used the Born approximation $u \simeq u^i$. The expansion coefficients $A_{\mu,s}^j$ are then obtained by substituting (25) into (§42). Using the window kernel in (§43) and applying the convolution theorem, we obtain

$$A_{\mu,s}^j = \langle O(\mathbf{r}), \Lambda_{\mu,s}^j(\mathbf{r}) \rangle \quad (26)$$

where

$$\Lambda_{\mu,s}^j(\mathbf{r}) = \frac{1}{2v_0 \cos \theta_n} F(t) \otimes \dot{\Phi}_{\mu,s}^{\mp}(\mathbf{r}, t)|_{t=t^i(\mathbf{r})} \quad (27a)$$

$$\simeq \frac{1}{2v_0 \cos \theta_n} \dot{\Phi}_{\mu,s}^{\mp}(\mathbf{r}, t)|_{t=t^i(\mathbf{r})} \quad (27b)$$

where $t^i(\mathbf{r}) \stackrel{\text{def}}{=} v_0^{-1} \hat{\mathbf{k}}^i \cdot \mathbf{r}$ is the arrival time of the incident pulse at \mathbf{r} , \otimes is a temporal convolution, $\dot{\Phi} \stackrel{\text{def}}{=} \partial_t \Phi$. The approximation in (27b) applies if the illumination is a short pulse.

The operation in (26) is a projection of $O(\mathbf{r})$ onto the spatial windows $\Lambda_{\mu,s}^j(\mathbf{r})$. We refer to it as the “data-object relation,” as it provides, within the Born model, a direct relation between the object and the beam-domain data $A_{\mu,s}^j$. The validity of this local model for the data is verified by the numerical results in the following (see Fig. 8).

Equation (26) is a localized version of the TD-DT identity (15), hence it is referred to as the *local time-domain diffraction tomography identity*. In order to understand this operation, we first clarify the properties of $\Lambda_{\mu,s}^j(\mathbf{r})$. Referring to Fig. 6, we express a point \mathbf{r} along the axis of $\Phi_{\mu,s}^{\mp}$ as $\mathbf{r} = \mathbf{x}_m + z_{b\mu}^{\mp} \hat{\mathbf{k}}_n^{\mp}$,

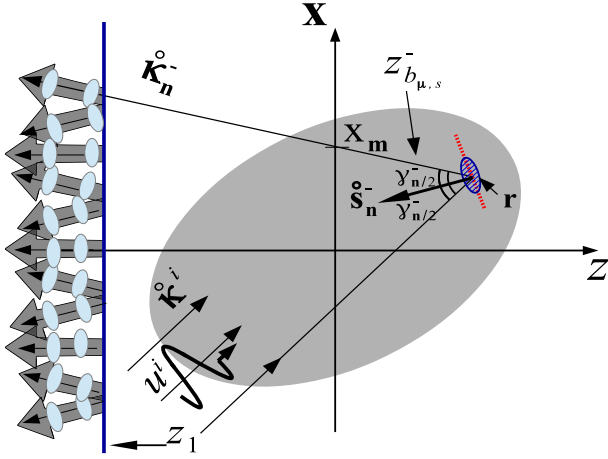


Fig. 6. Beam-domain data. The scattered field measured at the z_j plane (here, z_1) is expressed in (23) as a sum of PBs (blue ellipses) that propagate outside along the μ axes. Within the Born approximation, their amplitudes are related via (26) to local probing of $O(\mathbf{r})$ by the window kernels $\Lambda_{\mu,s}^j(\mathbf{r})$ of (27). As discussed after (32), these windows are slanted such that they bisect the angle γ_n^{\mp} between the direction of incidence and the scattered PB directions, and their distance $z_{b_{\mu,s}}^-$ from the point \mathbf{x}_m on the $z = 0$ plane is determined by t_s via (28). Mathematically, this sampling operation is identified as an LRT of O , whereas physically, it is interpreted as a localized version of the generalized Snell's law as shown in Fig. 4. In Part II [2], these scattered PBs will be backpropagated into the target domain to reconstruct the medium in the vicinity of \mathbf{r} .

where $\hat{\kappa}_n^{\mp} = (\xi_n, \mp \zeta_n)$ is the beam direction [see (5)] and $z_{b_{\mu}}^{\mp}$ denotes the coordinates along the axes (see Fig. §2). Note that, for a given t , this window is centered at $z_{b_{\mu}}^{\mp} = v_0(t - t_s)$, and substituting $t^i = v_0^{-1} \hat{\kappa}^i \cdot \mathbf{r}$ from (27b), we find that the location of the window center along the μ beam-axis is determined by t_s via (see Fig. 6)

$$z_{b_{\mu,s}}^{\mp} = (\hat{\kappa}^i \cdot \mathbf{x}_m - v_0 t_s) / (1 - \hat{\kappa}^i \cdot \hat{\kappa}_n^{\mp}) \quad (28)$$

so that the center of $\Lambda_{\mu,s}^j(\mathbf{r})$ is at

$$\mathbf{r} = \mathbf{x}_m + \hat{\kappa}_n^{\mp} (\hat{\kappa}^i \cdot \mathbf{x}_m - v_0 t_s) / (1 - \hat{\kappa}^i \cdot \hat{\kappa}_n^{\mp}). \quad (29)$$

Next, we calculate the transversal orientation of $\Lambda_{\mu,s}^j(\mathbf{r})$. Near the beam axis, the wavefront of $\Phi_{\mu,s}^{\mp}(\mathbf{r}, t)$ satisfies $\hat{\kappa}_n^{\mp} \cdot \mathbf{r} = v_0(t - t_s) + \xi_n \cdot \mathbf{x}_m$, where we neglected the wavefront curvature due to propagation (see (§35) with $\xi \approx \xi_n$). Inserting $t = t^i$ from (27b), we find that the center of $\Lambda_{\mu,s}^j(\mathbf{r})$ satisfies the relation

$$(\hat{\kappa}_n^{\mp} - \hat{\kappa}^i) \cdot \mathbf{r} = \xi_n \cdot \mathbf{x}_m - v_0 t_s. \quad (30)$$

In order to explain this relation, we refer to (14) and Fig. 6 and define

$$\hat{\mathbf{s}}_n^{\mp} = \frac{\hat{\kappa}_n^{\mp} - \hat{\kappa}^i}{2 \cos(\gamma_n^{\mp}/2)}, \quad \cos \gamma_n^{\mp} = -\hat{\kappa}^i \cdot \hat{\kappa}_n^{\mp} \quad (31)$$

such that $\hat{\mathbf{s}}_n^{\mp}$ is a unit vector that bisects the angle γ_n^{\mp} between $-\hat{\kappa}^i$ and $\hat{\kappa}_n^{\mp}$. Equation (30) can be cast as

$$\hat{\mathbf{s}}_n^{\mp} \cdot \mathbf{r} = (\xi_n \cdot \mathbf{x}_m - v_0 t_s) / 2 \cos(\gamma_n^{\mp}/2) = \text{const.} \quad (32)$$

Equations (29) and (32) describe the location and orientation of the medium-sampling window $\Lambda_{\mu,s}^j(\mathbf{r})$ in (26). As illustrated by the blue ellipses in Figs. 4 and 6, this window is localized along the μ -beam axis, and is orthogonal to the direction $\hat{\mathbf{s}}_n^{\mp}$ that bisects the angle γ_n^{\mp} between the direction of incidence $-\hat{\kappa}^i$ and the scattered PB direction $\hat{\kappa}_n^{\mp}$. Its location along this axis is determined by the time parameter t_s via (29). Thus, $\Lambda_{\mu,s}^j$ in (26) are identified as the LRT³ of $O(\mathbf{r})$ as schematized by the blue ellipses in Fig. 6.

Recalling the discussion after (15), the result in (26) has a cogent physical interpretation as a localized version of the generalized Snell's law. As schematized in Fig. 6, the local stratification of O at any given direction, which is expressed by the LRT of O (schematized by the blue ellipses in Fig. 6), gives rise to a reflected PB propagator (schematized by the light blue ellipses there) at an angle that equals the angle of incidence.

D. ID-PB Processing

As mentioned earlier, we use the ID-PB set because of its favorable properties mentioned in Section I (item 2c). The properties of the ID-PB wave-functions are discussed in Appendices §B and §C for 3-D and 2-D configurations, respectively. Specifically, explicit expressions for the propagators $\Psi_{\mu,s}^{\pm}(\mathbf{r}, t)$ are given in (§B5) and (§C4), while the dual (processing) propagators $\Phi_{\mu,s}^{\pm}(\mathbf{r}, t)$ are given in (§B6) and (§C5).

The ID-PB are the TD counterparts of the ID-GB which are used in the FD formulation of Section IV-A (see Appendix §A). As such, they are controlled by the frequency-independent collimation distance b . As explained in (§A2), once b is determined for a given application, it also determines the *optimal* frequency-independent beam-lattice parameters $(\bar{x}, \bar{\xi})$. In addition, the ID-PBs depend on the analytic filter function $\Upsilon(t)$ which is fully determined by the frequency bandwidth of the problem (see the parameters $\omega_{L,H}$ and $\Delta_{L,H}$ in Fig. §13; explicit expression for $\Upsilon(t)$ is given in [32, eq. (32)]). Finally, the ID-PBs in (§B5) and (§B6) are also controlled by the parameters (γ, α) : γ is typically taken to be 0, 1, 2, or 3, and its role is to switch the time-derivatives between the propagators $\Psi_{\mu,s}^{\pm}$ and the processing windows $\Phi_{\mu,s}^{\pm}$. α is typically taken to be 0 or $\pi/2$ and its role is to control the symmetry of the PB windows. The guidelines for choosing these parameters for a given application are discussed in Appendixes §B(c) and §C(b). The choice of these parameters for the present application of imaging is discussed after (34) and is also demonstrated in the numerical example of Section VI.

The medium-sampling windows $\Lambda_{\mu,s}^j(\mathbf{r})$ are expressed in (27) in terms of the propagators $\partial_t \Phi_{\mu,s}^{\mp}(\mathbf{r}, t)$. For 3-D

³A note on the terminology: we distinguish between the WRT and the LRT. The former, defined in (24) (see also (§33) and Fig. §7), is an operation on the space-time data in the (\mathbf{x}, t) domain, while the latter operates on the medium and is a function of space only. We use different names to distinguish between these transforms although both represent windowed-localization of the Radon transforms.

configurations, using the ID-PB functions $\Phi_{\mu,s}^\mp$ from (§B5) and (§B6), we obtain

$$\Lambda_{\mu,s}^j(\mathbf{r}) = \text{Re} \left\{ \sqrt{\frac{-iF_{\mu_1}}{z_{b_\mu} - iF_{\mu_1}} \frac{-iF_{\mu_2}}{z_{b_\mu} - iF_{\mu_2}}} \right. \\ \times \frac{(-1)^{\gamma+1} \bar{t} v_{\max}^2}{2\pi b v_0^2 \cos \theta_n \omega_{\max}^2} i e^{i\alpha} \Upsilon^{+(4-\gamma)} \left(\frac{\mathbf{k}^i \cdot \mathbf{r}}{v_0} \right. \\ \left. \left. - t_s - \frac{z_{b_\mu}}{v_0} - \frac{x_{b_{\mu_1}}^2/2v_0}{z_{b_\mu} - iF_{\mu_1}} - \frac{x_{b_{\mu_2}}^2/2v_0}{z_{b_\mu} - iF_{\mu_2}} \right) \right\}, \quad (33)$$

where the beam coordinates $(z_{b_\mu}, \mathbf{x}_{b_\mu})$ and the collimation lengths $F_{\mu_{1,2}}$ are defined in (§A5). Note that this expression applies for short illumination pulse, whereas for a general pulse, this result should be convolved with F as is (27a).

For 2-D configurations, we use the ID-PB functions $\Phi_{\mu,s}^\mp$ from (§C4) and (§C5), obtaining

$$\Lambda_{\mu,s}^j(\mathbf{r}) = \text{Re} \left\{ \sqrt{\frac{-iF_\mu}{z_{b_\mu} - iF_\mu}} \right. \\ \times \frac{(-1)^{\gamma+1} \bar{t} v_{\max}}{2\sqrt{\pi b v_0^3} \cos \theta_n \omega_{\max}} e^{i\alpha} e^{-i\frac{\pi}{4}} \\ \left. \times \Upsilon^{+(\frac{5}{2}-\gamma)} \left(\frac{\mathbf{k}^i \cdot \mathbf{r}}{v_0} - t_s - \frac{z_{b_\mu}}{v_0} - \frac{x_{b_\mu}^2/2v_0}{z_{b_\mu} - iF_\mu} \right) \right\}. \quad (34)$$

Note that this expression involves a fractional derivative of Υ as defined in (§C10).

1) *Choosing the Parameters (γ, α) : 3-D Case:* The following discussion regarding the choice of the parameters γ and α is based on the discussion in Appendix §B(c).

It is desired that the sampling windows $\Lambda_{\mu,s}^j$ will be collimated inside the tested object, hence we typically choose b to be comparable to or larger than the object's support. It follows that z_{b_μ} are smaller than $F_{\mu_{1,2}}$, hence the square roots in (33) or (34) are essentially one. It thus follows from (33) that $\Lambda_{\mu,s}^j \sim \text{Re} \{ i e^{i\alpha} \Upsilon^{+(4-\gamma)} \}$ up to some real multipliers. Thus, following the discussion after (§B6), using $\gamma = 0$ or 2 with $\alpha = \pi/2$ or $\gamma = 1$ or 3 with $\alpha = 0$ yields windows that are localized and symmetric about the axis. As demonstrated in Part II [2], these values also lead to imaging kernels with favorable properties.

Note that one may prefer windows that are antisymmetrical along their axis, thus sensing the *derivative* of the medium stratification along the beam axis. Such windows are obtained by using even γ with $\alpha = 0$ or odd γ with $\alpha = \pi/2$.

Next, we consider the structure of the space-time data processing windows $\Phi_{\mu,s}^\mp(\mathbf{r}, t)|_z$ in (24). These windows are given by (§B5) in conjunction with the upper term in (§B6). Assuming that the measurement planes z_j are in the far zone with respect to collimation length b , i.e., $|z_j| \gg b$, it follows that the argument of the square root in (§B5) is $-i$. It therefore follows that $\Phi_{\mu,s}^\mp \sim \text{Re} \{ e^{i\alpha} \Upsilon^{+(3-\gamma)} \}$ up to some real multipliers. It then follows that $\Phi_{\mu,s}^\mp$ have essentially the same properties as $\Lambda_{\mu,s}^j$ as discussed earlier. Specifically, if we use $\gamma = 0$ or 2 with $\alpha = \pi/2$ or $\gamma = 1$ or 3 with $\alpha = 0$ as indicated earlier, then $\Phi_{\mu,s}^\mp$ are spatially localized about the

beam axis, and are also localized and essentially symmetric about the t -axis.

2) *Choosing the Parameters (γ, α) : 2-D Case:* Likewise, for the 2-D case, we observe in (34) that $\Lambda_{\mu,s}^j \sim \text{Re} \{ e^{i\alpha - i\pi/4} \Upsilon^{+(\frac{5}{2}-\gamma)} \}$ up to some real multipliers. Then using the definition of the fractional derivative in (§C10), we find that $\Lambda_{\mu,s}^j \sim \text{Re} \{ e^{i\alpha} \Upsilon^{+(3-\gamma)}(t) \otimes 1/\sqrt{|t|} \}$. Noting that the convolution with $1/\sqrt{|t|}$ does not affect the symmetry of the signal, it follows that the preferred parameters here are $\gamma = 0$ or 2 with $\alpha = \pi/2$ or $\gamma = 1$ with $\alpha = 0$.

A specific example of these considerations is given in the numerical example of Section VI.

E. Section Summary

We defined the PBF expansion (23) of the scattered field, where the expansion coefficients $A_{\mu,s}^j$, referred to as the “beam-domain data,” are extracted from the measured data $u_j^s(\mathbf{x}, t)$ via the windowed transform in (24). This operation can be regarded, rather simplistically, as a WRT of $u_j^s(\mathbf{x}, t)$ over the z_j planes. Note though that the windows are actually more complicated than the simple schematization shown in Fig. §7, as the window has a propagation curvature. Furthermore, unlike the WRT, the windows are not structured upon a Cartesian phase-space lattice, but rather upon the beam skeleton, hence we refer to (24) as the PBF transform.

Next, we have demonstrated in (26) that within the Born approximation, $A_{\mu,s}^j$ are directly related to the projection of $O(\mathbf{r})$ onto the “medium sampling windows” $\Lambda_{\mu,s}^j(\mathbf{r})$ in (27). This projection has been shown in (29)–(32) to be an LRT (see footnote 3) of O at an angle that bisects the angle between the incident wave direction and the scattered PB direction, as schematized by the blue ellipses in Figs. 4 and 6. Thus, the result in (26) is a localized version of the TD-DT identity (15). As discussed after (32), this result has a cogent physical interpretation as a localized version of the generalized Snell's law.

Finally, in Section V-D, we considered the special case of the ID-PB which are our favorable basis functions for propagation and data processing. We derived explicit expressions for these wave-functions and discussed how the various parameters that control them should be chosen by the wave modeler.

VI. NUMERICAL EXAMPLE

To illustrate the local phenomenology and interpretation of the beam-domain data (the forward problem), we consider the specific configuration described in the following. These data will be used in Part II [2] for the reconstruction (the inverse problem).

The data processing is carried out using the ID-PB windows, which are given in Appendixes §A–§C. In Sections VI-B, we demonstrate the considerations for choosing the parameters that control these windows.

A. Physical Configuration

We consider the quasi-layered medium in a 2-D coordinate frame $\boldsymbol{\rho} = (x, z)$ shown in Fig. 7. It consists of several shifted

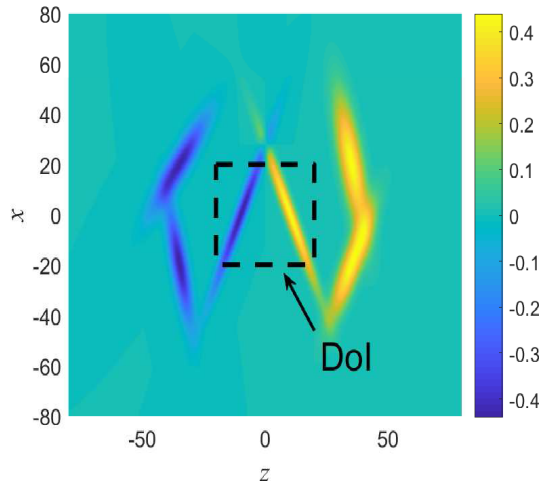


Fig. 7. Tested medium in (35). The DoI is marked by the black rectangle.

and tilted 2-D Gaussians tagged by the index $l = 1, 2, \dots$, which are centered at (x_l, z_l) and are tilted at an angle θ_l . They are given by

$$O(\mathbf{r}) = \sum_l O_l \exp \left\{ -\eta_1^2/2\sigma_{1l}^2 - \eta_2^2/2\sigma_{2l}^2 \right\} \quad (35)$$

where O_l is the value of the contrast $n^2 - 1$ at the center of the Gaussian, (η_1, η_2) are the tilted coordinate about the center (x_l, z_l) , i.e.,

$$\begin{pmatrix} \eta_1 \\ \eta_2 \end{pmatrix} = \begin{pmatrix} \cos \theta_l & -\sin \theta_l \\ \sin \theta_l & \cos \theta_l \end{pmatrix} \begin{pmatrix} x - x_l \\ z - z_l \end{pmatrix} \quad (36)$$

and $(\sigma_{1l}, \sigma_{2l})$ are the Gaussian widths along these coordinates. It is also assumed that $\sigma_{1l} \gg \sigma_{2l}$ so that the medium has the quasi-layer structure in Fig. 7. The values of these parameters for the medium in Fig. 7 are listed in Table I.

For simplicity, the units are normalized such that the background wave-speed $v_0 = 1$. Note that the contrast is of order 40%. The quality of reconstruction of this relatively large contrast will be demonstrated in [2, Sec. V.D]. The DoI $\mathbf{r} \in [-20, 20] \times [-20, 20]$ is marked by the black rectangle in Fig. 7.

The medium is illuminated by the pulsed plane wave (11) with $\hat{\mathbf{k}}^i = \hat{\mathbf{z}}$. The pulselength T_0 of F is chosen to be short enough in order to resolve the details of the layers which are of order 1 (see Table I). We, therefore, choose $\Omega = [\omega_{\min}, \omega_{\max}] = [0.1, 1]$ giving $T_0 \approx 2\pi$. We consider only the reflection data at $z = z_l = -150$.

B. Choosing the Frame and Propagator Parameters

As noted in Section V-D, we use the ID-PB propagators $\Psi_{\mu,s}^\pm(\mathbf{r}, t)$ and $\Phi_{\mu,s}^\pm(\mathbf{r}, t)$, which are controlled by the frequency-independent collimation length b . For best localization, we choose $b = 50$ such that the beams are collimated inside the support of O , while maintaining a good collimation condition $kb \gg 1$. The beamwidth of the beams that pass inside the DoI is $W_0 \simeq \sqrt{b/k_{\max}} = \sqrt{50}$ [see (§A6a)]. Once b is chosen, the beam-lattice is calculated by inserting b and $\nu_{\max} = 0.3$ into (§A2), yielding $(\bar{x}, \bar{z}) \approx (9.71, 0.195)$.

TABLE I
PARAMETERS OF THE MEDIUM IN FIG. 7

l	n_l	x_l	z_l	θ_l	σ_{1l}	σ_{2l}
1	1.2	0	10	$\pi/9$	$10\sqrt{5}$	$\sqrt{5/2}$
2	0.75	0	-10	$-\pi/9$	$10\sqrt{5}$	$\sqrt{5/2}$
3	1.2	20	35	$\pi/18$	$\sqrt{350}$	$\sqrt{10}$
4	0.75	-20	-35	$\pi/18$	$5\sqrt{10}$	$\sqrt{5}$
5	1.2	-20	35	$-\pi/9$	$5\sqrt{10}$	$\sqrt{15/2}$
6	0.75	20	-35	$-\pi/6$	$10\sqrt{2}$	$\sqrt{15/2}$

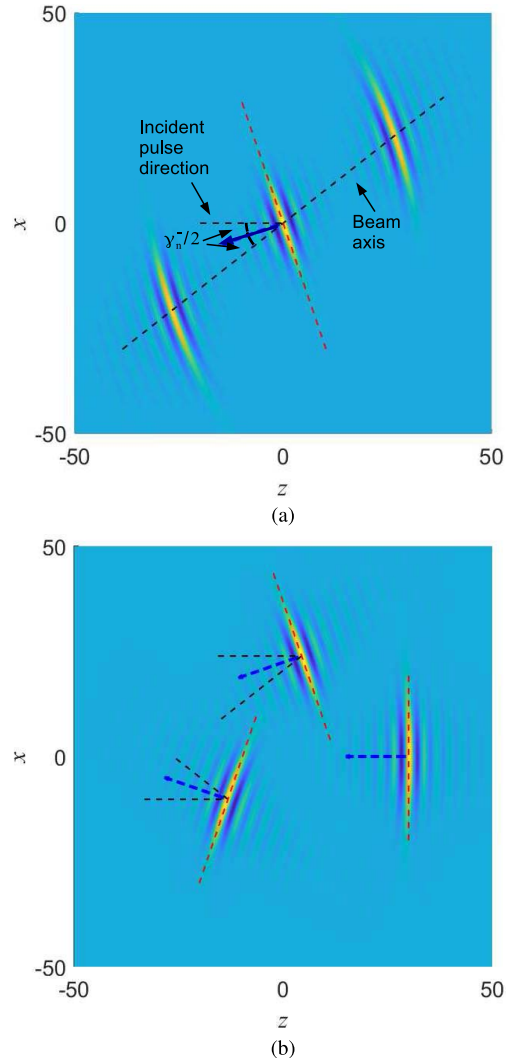


Fig. 8. Medium sampling windows $\Lambda^j(\mathbf{r})$. (a) Fixed μ and several values of s . (b) Several values of μ and s .

As discussed in Section V-D, the ID-PBs depend on the analytic filter function $\Upsilon^+(t)$ for complex t and on the parameters (γ, α) . $\Upsilon^+(t)$ is taken from [32, eq. (32b)], where for the present problem, we chose $\omega_L = \omega_{\min} = 0.1$, $\omega_H = 5\omega_{\max} = 5$, and $\Delta_L = \Delta_H = 0.05$.

The considerations for choosing γ and α are discussed after (34). Specifically, for the 2-D examples here, we used $\gamma = 1$ and $\alpha = 0$, so that the medium-sampling windows $\Lambda_{\mu,s}^j$ are localized and symmetric about their axes, as required.

Few examples of these windows are plotted in Fig. 8: In Fig. 8(a), they are depicted for a fixed μ and several values

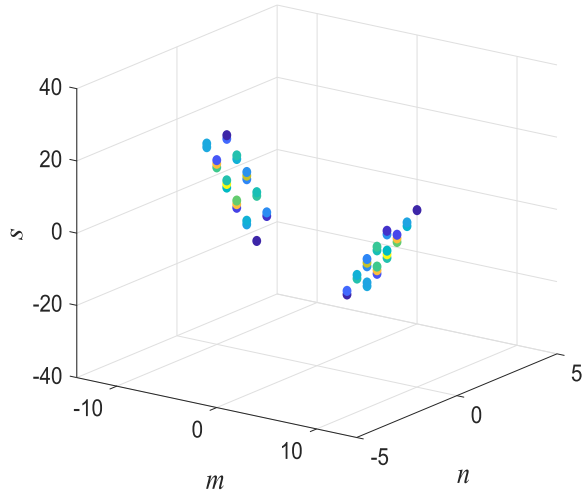


Fig. 9. Beam-domain data $A_{\mu,s}^{j=1}$ in the discrete 3-D (m, n, s) phase space. Only the dominant coefficients are shown with the magnitude tagged by colors, from brightest to darkest.

of s , demonstrating how the window moves along the beam axis such that they are tilted in the $\hat{\mathbf{s}}_n^-$ direction (blue arrows) that bisects the angle γ_n^- between the beam axis and the direction of incidence $-\hat{\mathbf{z}}$, as explained after (32). In Fig. 8(b), these windows are depicted for several values of μ and s . Note that we have plotted the actual windows in (27a), obtained after convolving the generic windows of (33) and (34) by the excitation pulse $F(t)$ [see comment after (33)]. Since, as noted earlier, the spectrum of $F(t)$ in this example is truncated at $\omega_{\max} = 1$, whereas the spectrum of the generic windows extends up to $\omega_n = 5$ where it tapers smoothly to zero, and these windows have a few ripples along the beam axis which can readily be discerned in the figures.

Finally, we note that the ID-PB windows $\Phi_{\mu,s}^{\pm}(\mathbf{r}, t)|_{z_j}$ which are used in the data processing (24) are given by (§C4) wherein $\Upsilon^+(t)$ is replaced by the upper expression in (§C5) and we also use all the other parameters discussed earlier.

C. Beam-Domain Scattering Data: Data–Object Relation

Finally, we explore the beam-domain data $A_{\mu,s}^{j=1}$ calculated via (24) using the processing windows $\Phi_{\mu,s}^{\pm}(\mathbf{r}, t)|_{z_j}$ discussed earlier. For clarity, we present only the contributions corresponding to the part of the object inside the DoI (the black rectangle in Fig. 7) and retain only the beams passing within three beamwidths away from the DoI. Fig. 9 depicts these coefficients in the 3-D discrete domain (m, n, s) corresponding to the spatial shift x_m , spectral tilt ζ_n , and temporal shift t_s . The coefficients are threshold at a level of 10%, with the magnitude tagged by colors, from the brightest to the darkest.

The results verify the theoretical model for the coefficients in (26) and (27), using the medium-sampling windows $\Lambda_{\mu,s}^j(\mathbf{r})$ of (34). As explained there, the coefficients constitute a local Radon transform of $O(\mathbf{r})$ and therefore are localized around $\theta_n \simeq \pm 40^\circ$, representing a bistatic reflection by the layers $l = 1, 2$ in Table I whose inclinations are $\pm 20^\circ$, respectively. This interpretation is illustrated in Fig. 10. The (m, s) coordinates

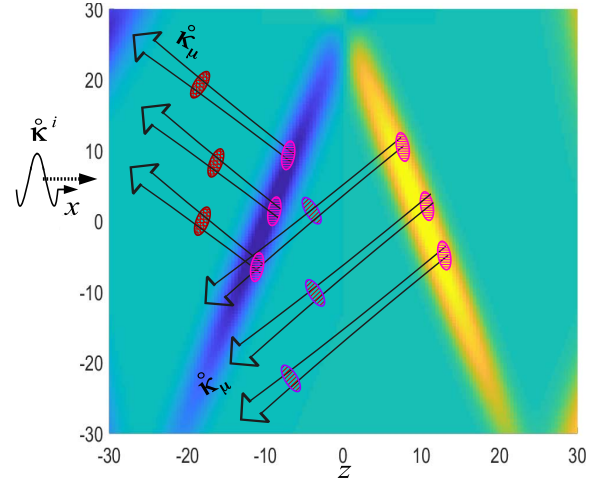


Fig. 10. Physical interpretation of the dominant coefficients of the data in Fig. 9 in terms of the LRT of $O(\mathbf{r})$ and local Snell's law.

correspond to the (x, z) coordinates of the reflection points as explained in (29)–(32).

VII. SUMMARY AND CONCLUSION

This two-part sequence is concerned with UWB beam-based tomographic inverse scattering. We considered two formulations: a multi-FD formulation in Section IV and a time formulation in Section V. They are structured, respectively, upon the BFs (Section IV-A) and the PBFs (Section V-A) that constitute overcomplete frames everywhere in the propagation domain, and thus can be used for local phase-space expansion of the medium heterogeneity and of the locally scattered fields. A unique feature of these frames, denoted as ID, is that they utilize the same phase-space skeleton of beam waves.

Both inversion schemes consist of two phases: a *preprocessing phase*, where the scattering data is expanded as a sum of beam propagators whose amplitudes, referred to as the “beam-domain data,” are extracted from the data via local beam-based transforms, and an *imaging phase*, where this data is backpropagated and used to reconstruct the medium. These phases are dealt with, respectively, in this article and in Part II [2].

The beam-based transforms that are used to calculate the beam-domain data are defined in (17) and (24) for the FD and TD formulations, respectively. In these expressions, the local phase-space processing windows $\hat{\Phi}_{\mu,s}^{\pm}(\mathbf{r}, \omega)$ and $\Phi_{\mu,s}^{\pm}(\mathbf{r}, t)$, are the dual BF and the dual PBF, respectively, while $\hat{u}_j^s(\mathbf{x}, \omega)$ and $u_j^s(\mathbf{x}, t)$ are the scattering data over the z_j measurement planes, $j = 1, 2$ (see Fig. 1). Explicit expressions for the ID-BF functions, along with guidelines for choosing the various parameters that control them, are given in Appendixes §A–§C of [1] and in the numerical examples here and in [1].

Analytical models for the beam-domain data were derived by utilizing the Born approximation of the data. Specifically, it has been shown in (26) that the beam-domain data can be described by projecting the medium function on a set of phase-space window functions $\Lambda_{\mu,s}^j(\mathbf{r})$ corresponding to the

propagated PB waves via (27b) (see Fig. 6). As discussed in (28)–(32), these sampling windows are inclined such that they bisect the angle between the direction of incidence and the scattered PB direction, a relation that has a cogent physical interpretation in terms of a *local Snell's law*. Mathematically, this projection constitutes an LRT of the medium, hence it can be utilized for local reconstruction of the medium as will be done in Part II [2]. This relation is the *beam-domain* counterpart of the *time-domain diffraction tomography identity* in (15). Further conclusions are deferred to the overall summary of this article in [2].

A. DERIVATION OF (7)

We use the spectral representation of $\hat{G}(\mathbf{r}, \mathbf{r}')$

$$\hat{G}(\mathbf{r}, \mathbf{r}') = \left(\frac{k}{2\pi}\right)^2 \int d^2\xi \frac{1}{-2ik\zeta} e^{ik(\xi \cdot (\mathbf{x}-\mathbf{x}') + \zeta|z-z'|)} \quad (\text{A1})$$

and insert it into (6) together with (5), obtaining

$$\begin{aligned} \hat{u}_j^s(\mathbf{x}) &= \left(\frac{k}{2\pi}\right)^2 \int d^3r' O(\mathbf{r}') \int d^2\xi \\ &\times \frac{k}{-2i\zeta} e^{ik(\xi \cdot (\mathbf{x}-\mathbf{x}') + \zeta|z_j-z'| + \xi^i \cdot \mathbf{x}' + \zeta^i z')} \\ &= \left(\frac{k}{2\pi}\right)^2 \int d^2\xi e^{ik(\xi \cdot \mathbf{x} + \zeta z_j)} \frac{k}{-2i\zeta} \int d^3r' \\ &\times O(\mathbf{r}') e^{-ik((\xi - \xi^i) \cdot \mathbf{x}' + (\zeta - \zeta^i) z')}. \end{aligned} \quad (\text{A2})$$

Comparing (A2) to (4) and using (8) for spectral values in the visible space $|\xi| < 1$, we end up with the result of (7).

REFERENCES

- [1] R. Tuvi, E. Heyman, and T. Melamed, "Beam frame representation for ultrawideband radiation from volume source distributions: Frequency-domain and time-domain formulations," *IEEE Trans. Antennas Propag.*, vol. 67, no. 2, pp. 1010–1024, Feb. 2019.
- [2] R. Tuvi, E. Heyman, and T. Melamed, "UWB beam-based local diffraction tomography—Part II: The inverse problem," *IEEE Trans. Antennas Propag.*, vol. 68, no. 10, pp. 7158–7169, Oct. 2020.
- [3] A. J. Devaney, "A filtered backpropagation algorithm for diffraction tomography," *Ultrason. Imag.*, vol. 4, no. 4, pp. 336–350, Oct. 1982.
- [4] A. J. Devaney et al., "Diffraction tomography," in *Inverse Methods in Electromagnetic Imaging*, W. M. Boerner, Ed. Dordrecht, The Netherlands: D. Reidel, 1985, pp. 1107–1135.
- [5] A. J. Devaney, "Inversion formula for inverse scattering within the born approximation," *Opt. Lett.*, vol. 7, no. 3, p. 111, Mar. 1982.
- [6] A. J. Devaney, *Mathematical Foundations of Imaging, Tomography and Wavefield Inversion*. Cambridge, U.K.: Cambridge Univ. Press, 2012.
- [7] K. J. Langenberg, "Applied inverse problems for acoustic, electromagnetic and elastic wave scattering," in *Basic Methods Tomography Inverse Problems* (Malvern Physics Series), P. C. Sabatier, Ed. Bristol, U.K.: Adam Hilger, 1987.
- [8] T. Melamed, Y. Ehrlich, and E. Heyman, "Short-pulse inversion of inhomogeneous media: A time-domain diffraction tomography," *Inverse Problems*, vol. 12, no. 6, pp. 977–993, Dec. 1996.
- [9] T. Melamed, E. Heyman, and L. B. Felsen, "Local spectral analysis of short-pulse excited scattering from weakly inhomogeneous media. I. Forward scattering," *IEEE Trans. Antennas Propag.*, vol. AP-47, no. 4, pp. 1208–1217, Jul. 1999.
- [10] T. Melamed, E. Heyman, and L. B. Felsen, "Local spectral analysis of short-pulse excited scattering from weakly inhomogeneous media. II. Inverse scattering," *IEEE Trans. Antennas Propag.*, vol. 47, no. 7, pp. 1218–1227, Jul. 1999.
- [11] B. Rao and L. Carin, "Beam-tracing-based inverse scattering for general aperture antennas," *J. Opt. Soc. Amer. A, Opt. Image Sci.*, vol. 16, no. 9, pp. 2219–2231, Sep. 1999.
- [12] Y.-S. Yoon and M. G. Amin, "High-resolution Through-the-Wall radar imaging using beamspace MUSIC," *IEEE Trans. Antennas Propag.*, vol. 56, no. 6, pp. 1763–1774, Jun. 2008.
- [13] T. Heilpern, A. Shlivinski, and E. Heyman, "Back-propagation and correlation imaging using phase-space Gaussian-beams processing," *IEEE Trans. Antennas Propag.*, vol. 61, no. 11, pp. 5676–5688, Nov. 2013.
- [14] T. Heilpern and E. Heyman, "MUSIC imaging using phase-space Gaussian-beams processing," *IEEE Trans. Antennas Propag.*, vol. 62, no. 3, pp. 1270–1281, Mar. 2014.
- [15] G. Lahav and T. Melamed, "Evolutionary algorithms applications for inverse scattering using Gaussian beams," in *Proc. URSI Int. Symp. Electromagn. (EMTS)*, Aug. 2016, pp. 60–62.
- [16] N. R. Hill, "Gaussian beam migration," *Geophysics*, vol. 55, no. 11, pp. 1416–1428, Nov. 1990.
- [17] N. R. Hill, "Prestack Gaussian-beam depth migration," *Geophysics*, vol. 66, no. 4, pp. 1240–1250, Jul. 2001.
- [18] T. K. Wang and D. A. Waltham, "Seismic modelling over 3-D homogeneous layered structures—summation of Gaussian beams," *Geophys. J. Int.*, vol. 122, no. 1, pp. 161–174, Jul. 1995.
- [19] R. L. Nowack, "Dynamically focused Gaussian beams for seismic imaging," *Int. J. Geophys.*, vol. 2011, May 2011, Art. no. 316581.
- [20] L. Chen, R.-S. Wu, and Y. Chen, "Target-oriented beamlet migration based on Gabor-Daubechies frame decomposition," *Geophysics*, vol. 71, no. 2, pp. S37–S52, Mar. 2006.
- [21] S. H. Gray and N. Bleistein, "True-amplitude Gaussian-beam migration," *Geophysics*, vol. 74, no. 2, pp. S11–S23, Mar. 2009.
- [22] N. Bleistein and S. H. Gray, "Amplitude calculations for 3D Gaussian beam migration using complex-valued traveltimes," *Inverse Problems*, vol. 26, no. 8, Aug. 2010, Art. no. 085017.
- [23] K. Žáček, "Gaussian packet prestack depth migration," in *Seismic Waves in Complex 3-D Structures*, vol. 15. Prague, Czechia: Dep. Geophys., Charles Univ., 2005, pp. 29–48. [Online]. Available: <http://sw3d.mff.cuni.cz>
- [24] K. Žáček, "Decomposition of the wave field into optimized Gaussian packets," *Studia Geophysica et Geodaetica*, vol. 50, no. 3, pp. 367–380, Jul. 2006.
- [25] L. Klimeš, "Stochastic wavefield inversion using the sensitivity Gaussian packets," in *Seismic Waves Complex 3-D Structure*, vol. 18. Prague, Czechia: Dep. Geophys., Charles Univ., 2008, pp. 71–85.
- [26] C. Hu and P. L. Stoffa, "Slowness-driven Gaussian-beam prestack depth migration for low-fold seismic data," *Geophysics*, vol. 74, no. 6, pp. WCA35–WCA45, Nov. 2009.
- [27] M. M. Popov, N. M. Semtchenok, P. M. Popov, and A. R. Verdel, "Depth migration by the Gaussian beam summation method," *Geophysics*, vol. 75, no. 2, pp. S81–S93, Mar. 2010.
- [28] E. Heyman, "Pulsed beam propagation in inhomogeneous medium," *IEEE Trans. Antennas Propag.*, vol. 42, no. 3, pp. 311–319, Mar. 1994.
- [29] E. Heyman and L. B. Felsen, "Gaussian beam and pulsed-beam dynamics: Complex-source and complex-spectrum formulations within and beyond paraxial asymptotics," *J. Opt. Soc. Amer. A, Opt. Image Sci.*, vol. 18, no. 7, pp. 1588–1611, Jul. 2001.
- [30] A. Shlivinski, E. Heyman, A. Boag, and C. Letrou, "A phase-space beam summation formulation for wideband radiation," *IEEE Trans. Antennas Propag.*, vol. 52, no. 8, pp. 2042–2056, Aug. 2004.
- [31] A. Shlivinski, E. Heyman, and A. Boag, "A phase-space beam summation formulation for ultrawide-band radiation. II: A multiband scheme," *IEEE Trans. Antennas Propag.*, vol. 53, no. 3, pp. 948–957, Mar. 2005.
- [32] A. Shlivinski, E. Heyman, and A. Boag, "A pulsed beam summation formulation for short pulse radiation based on windowed radon transform (WRT) frames," *IEEE Trans. Antennas Propag.*, vol. 53, no. 9, pp. 3030–3048, Sep. 2005.
- [33] I. Daubechies, *Ten Lectures on Wavelets* (Regional Conference Series in Applied Mathematics), vol. 61. Philadelphia, PA, USA: SIAM, 1992.
- [34] M. Leibovich and E. Heyman, "Beam summation theory for waves in fluctuating media. Part I: The beam frame and the beam-domain scattering matrix," *IEEE Trans. Antennas Propag.*, vol. 65, no. 10, pp. 5431–5442, Aug. 2017.
- [35] M. Leibovich and E. Heyman, "Beam summation theory for waves in fluctuating media. Part II: Stochastic field representation," *IEEE Trans. Antennas Propag.*, vol. 65, no. 10, pp. 5443–5452, Oct. 2017.
- [36] R. Tuvi, Z. Zhao, and M. K. Sen, "Multi frequency beam-based migration in inhomogeneous media using windowed Fourier transform frames," *Geophys. J. Int.*, accepted for publication.
- [37] E. Heyman, "Time-dependent plane-wave spectrum representations for radiation from volume source distributions," *J. Math. Phys.*, vol. 37, no. 2, pp. 658–681, 1996.

- [38] S. R. Dean, *The Radon Transform and Some of Its Applications*. New York, NY, USA: Wiley, 1983.
- [39] A. Schatzberg and A. J. Devaney, "Super-resolution in diffraction tomography," *Inverse Problems*, vol. 8, no. 1, pp. 149–164, Feb. 1992.



Ram Tuvi was born in Holon, Israel, in 1982. He received the B.Sc. and M.Sc. degrees (*cum laude*) in electrical and computer engineering from the Ben-Gurion University of the Negev, Beersheba, Israel, in 2010 and 2013, respectively, and the Ph.D. degree from the School of Electrical Engineering, Tel Aviv University, Tel Aviv, Israel, in 2019.

He is currently a Post-Doctoral Fellow with the group of Prof. M. K. Sen at the Institute for Geophysics, University of Texas at Austin, Austin, TX, USA. His research interests include electromagnetics

and geophysics, analytical and numerical techniques in wave theory, scattering, and inverse scattering.



Ehud Heyman (Life Fellow, IEEE) was born in Tel Aviv, Israel, in 1952. He received the B.Sc. degree (*summa cum laude, Valedictorian*) in electrical engineering from Tel Aviv University, Tel Aviv, in 1977, the M.Sc. degree (Hons.) in electrical engineering from the Technion-Israel Institute of Technology, Haifa, Israel, in 1979, and the Ph.D. degree in electro-physics from the Polytechnic Institute of New York, New York, NY, USA, in 1982.

While at the Polytechnic Institute of New York, he was a Rothschild Fellow, a Fullbright Fellow, and a Hebrew Technical Institute Fellow. In 1983, he joined the Department of Physical Electronics, Tel Aviv University, where he is currently a Professor and the incumbent of the Jokel Chair of Electromagnetics. He served as the Department Head, the Founding Head of the School of Electrical Engineering from 2002 to 2005, and the Dean of Engineering from 2005 to 2014. He has published over 120 refereed journal articles and was an invited speaker at many international conferences. His research interests involve analytic methods in wave theory, including asymptotic and time-domain techniques for propagation and scattering, beam and pulsed-beam techniques, short-pulse antennas, inverse scattering, target identification, imaging and synthetic aperture radar, and propagation in random medium.

Dr. Heyman is a fellow of the IEEE Antennas and Propagation Society, a member of Sigma Xi, and the Chairman of the Israeli National Committee for Radio Sciences (URSI). He was a recipient of the Balthasar van der Pol Gold Medal Award of URSI for the year 2011. He was an Associate Editor of the IEEE Press Series on Electromagnetic Waves and the IEEE TRANSACTIONS ON ANTENNAS AND PROPAGATION.



Timor Melamed (Senior Member, IEEE) was born in Tel-Aviv, Israel, in January 1964. He received the B.Sc. degree (*magna cum laude*) in electrical engineering and the Ph.D. degree from Tel-Aviv University, Tel-Aviv, in 1989 and 1996, respectively.

From 1996 to 1998, he held a post-doctoral position at the Department of Aerospace and Mechanical Engineering, Boston University, Boston, MA, USA, and collaborated with Prof. L. B. Felsen. He is currently with the School of Electrical and Computer Engineering, Ben-Gurion University of the Negev, Be'er Sheva, Israel. His main fields of interest include propagation and scattering of waves, analytical methods in the time domain, scattering from moving objects, and beam methods.